Universiteit Utrecht

Nikhef

Bachelor thesis

Characterisation of a Clinical Calibration Phantom for Mammography using a Medipix3RX Detector

Author:
Amber van Keeken
Study: Physics & Astronomy

Supervisors:
André Mischke
Utrecht University
and
John Idárraga
Nikhef Amsterdam

15 June 2016

Abstract

This report presents the implementation and validation of software oriented towards image analysis in the field of mammography. This software was used to assess the performance of a new detector based on the Medipix3RX chip, that allows spectroscopic imaging, which may help to reduce radiation dose on the patient. The visibility of early signs of breast cancer, microcalcifications, mimicked on a calibration phantom, has been quantified by calculation of the so-called contrast-to-noise ratio. This calculation, as well as a procedure to determine the location of a signal, was implemented in the analysis software. It has been shown that the contrast-to-noise ratio agrees quite well with expectations. The software has proven to be a useful tool in characterisation and will be used in future testing.

Contents

1 Introduction **1**
1.1 Microcalcifications . . . 1
1.2 Medipix3RX ASIC . . . 2
1.2.1 Charge summing mode . . . 2
1.2.2 Spectroscopic mode . . . 3

2 Experimental setup **5**
2.1 X-ray source . . . 5
2.2 Test object . . . 5
2.3 Medipix3RX . . . 5
2.4 Software . . . 7

3 Imaging analysis techniques **9**
3.1 Corrections . . . 9
3.1.1 Open beam correction . . . 9
3.1.2 Beam hardening correction . . . 9
3.2 Contrast-to-noise ratio . . . 11
3.3 Kernel density function . . . 12

4 Phantom characterisation **13**
4.1 Method . . . 13
4.2 Results . . . 13

5 Conclusion **19**
5.1 Discussion . . . 19
5.2 Outlook . . . 21

Appendices **25**

A X-ray imaging **25**
A.1 Production of x-rays . . . 25
A.2 Absorption of x-rays . . . 27
A.3 Detection of x-rays . . . 27

B Implemented functionalities **31**
B.1 Region of interest . . . 31
B.2 Profile dialog in depth . . . 31
B.3 Possible improvements and extensions . . . 33

Chapter 1

Introduction

Sadly, breast cancer is still a leading cause of death for women. It is responsible for 30% of cancer cases among women in Europe [Karsa et al., 2008]. European health care recommends women between the age of 50 and 69 to screen the breasts regularly even when not showing any symptoms [The Council of the European Union, 2003], since early detection of signs of cancer can significantly increase the effectivity of treatment.
The most used screening technique after a clinical breast exam is mammography. Mammography is a field of x-ray imaging[1] in which images of the breast are taken to find any indications of breast cancer. A mammogram can detect a lump before it can be felt in breast exams, as well as microcalcifications and other abnormalities.
One disadvantage of mammography is the high false negative rate. Mammograms can show signs of early cancer even though these abnormalities will never result in malignant tumors and the patient never gets cancer. This causes unnecessary biopsies, which increases stress on the patient and the cost of the breast screening program.
Another disadvantage is of course the use of ionizing radiation. This radiation destroys body cells and might cause induced tumors. It is crucial therefore to reduce the radiation dose per imaging process as much as possible.
A new detector has been developed, which allows for spectroscopic x-ray imaging [Schioppa, 2014] and could identify materials such as calcium in breast tissue. Since the detector creates multiple images of different energy at once, the radiation dose on a patient can be reduced significantly.

This research project will focus on the performance of this new detector based on the Medipix3RX chip, as a photon-counting detector. Aside from further exploring the possibilities of colour x-ray imaging, its basic performance should be tested. The main effort of this research project has been put in the development of the software to be used in analysing the data. In the following sections, the objects of interest will be introduced as well as the detector that was tested. The software will be discussed briefly in chapter 2 along with the setup used to test the detector. The software needed for the analysis will be discussed in chapter 3, after which the results are presented.

1.1 Microcalcifications

Tiny clusters of calcium are called microcalcifications. They can differ in shape and size from 1 mm spheres to larger shell−like structures. Microcalcifications (MCs) can be an early sign of malignant carcinomas or other types of invasive cancer. Around 40 percent of breast cancers show MCs, often as the only features on a mammogram to indicate the presence of a tumor. Though there is no consensus about the direct correlation between MCs and the occurence of cancer, since MCs are also often found in benign tissue [Naseem et al., 2015]. Research has lead to the ability to at least distinguish microcalcifications that are definitely benign and do not need a biopsy, see Nalawade

[1] For more on x-ray imaging, see appendix A.3.

[2009]. MCs do however help in cancer prognosis, as there are strong associations between them and poor prognostic indicators[2]. For more information about recent research and an extensive correlation study see Naseem et al. [2015].
Either way, among other findings, microcalcifications deem it appropriate for a patient to get more regular check ups [Shetty, 2015] or undergo either ultrasound, MRI imaging or a biopsy to get more information about the nature of the anomaly. It is therefore important for mammography equipment to be able to resolve these tiny density variations. The equipment must be able to show these variations to the physicians using it.

1.2 Medipix3RX ASIC

The Medipix3RX-based detector is a photon counting detector developed at CERN to be used in medical imaging and offers the possibility of getting high quality images with a low dose, by permitting colour imaging and dead time free operation. These promising features have been shown by Ballabriga et al. [2013] and Schioppa [2014].
The Medipix3RX ASIC[3] is an active−pixel detector readout chip that is designed to be connected to a segmented semiconductor sensor [Ballabriga et al., 2011, Medipix collaboration CERN, 2016]. The fact that the readout chip and the semiconductor sensor are manufactured seperately, makes the Medipix3RX detector a so-called hybrid detector. This means it's possible for the two parts to be optimized seperately and leaves the possibility to connect the readout chip to other sensor materials for other applications. The semiconductor sensor is in this case a 500 µm silicon layer that is bump bonded to the readout chip, as illustrated in figure 1.1. The chip has 256×256 pixels of 55 µm. The detector is an active−pixel image sensor using CMOS[4] technology, meaning each pixel has its own or circuitry and can perform simple operations on pixel−level. Most important are the two discriminators and two 12−bit counters that can be found on each pixel. These allow for two configurations. The chip can work in continuous read/write mode in which one counter is read out while the other counts, thus eliminating dead-time. Alternatively, the chip can use the two counters in sequential read-write mode, using two different thresholds set by the associated discriminators. This way both a lower and upper energy threshold can be set, allowing the user to eliminate noise and count photons of a particular part of the x-ray energy spectrum[5].

1.2.1 Charge summing mode

Apart from each pixel performing operations on the incoming signal, pixels can also compare signals. The Medipix3 chip uses this inter−pixel communication to differentiate between multiple photons of low energy in seperate pixels and a photon of higher energy whose generated charge has been spread out over multiple pixels. When an incoming photon deposits its energy near the edges of a pixel, the generated electron-hole cloud drifts downward, but also diffuses. This might cause some of the charge to fall in the neighbouring pixels. To prevent this from looking like multiple incoming photons in neighbouring pixels and thus distorting the original absorption pattern, charge summing is used. In *charge summing mode* the charge received by four pixels in a 2×2 square is summed and allocated to the pixel that received the most charge on an event-by-event basis. This is illustrated in figure 1.2, in which the charge generated by one photon is received by four pixels. The result is a single pixel that detects a photon instead of all four pixels.
Without this feature, in *single pixel mode*, the spectrum of a single pixel would look like the blue line in figure 1.3. The red line shows the spectrum in charge summing mode. The distortion towards lower energies has been removed. This will prove to be useful in

[2] *Poor* in this context does not mean that the indicators are lacking, but that they indicate a negative diagnosis.
[3] Application Specific Integrated Circuit.
[4] Complementary Metal–Oxide–Semiconductor.
[5] Hence the name *colour imaging*.

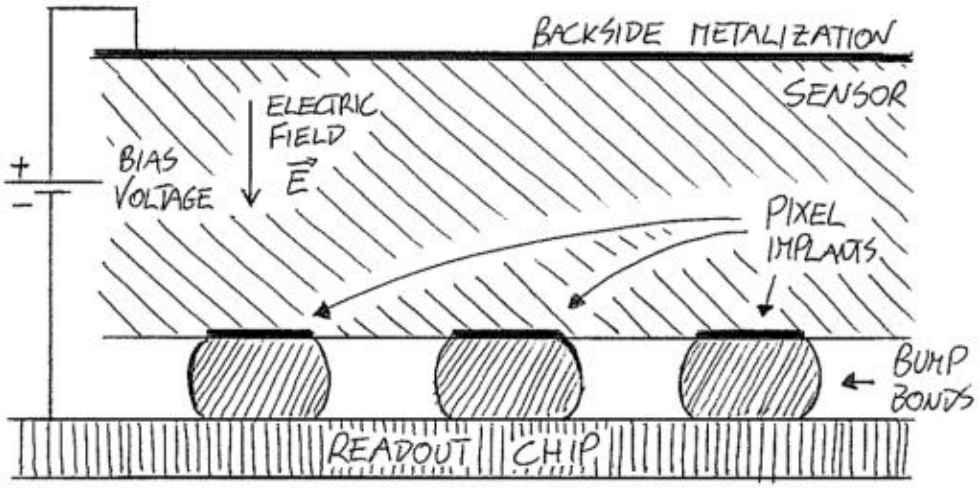

Figure 1.1 – Principle of operation of a hybrid semiconductor pixel detector. [Image from Schioppa [2014].]

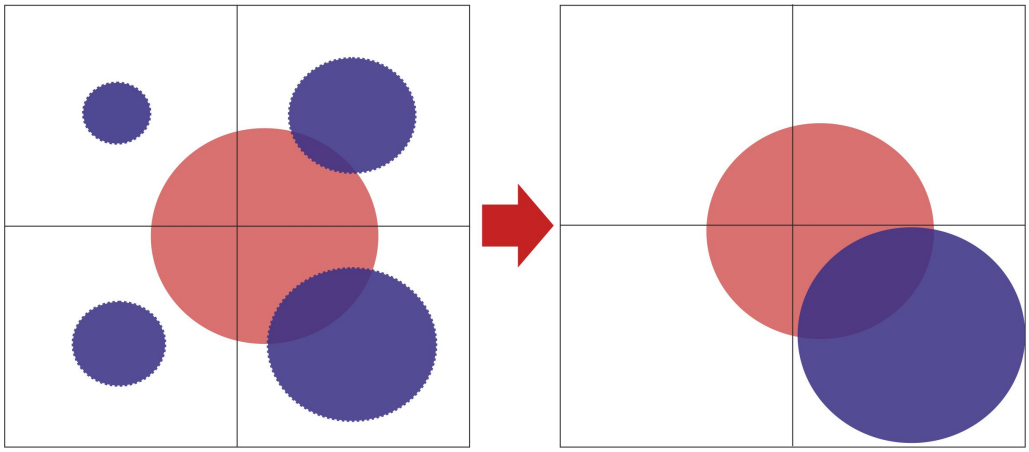

Figure 1.2 – Four pixels sharing an incoming charge (in red). Left: the situation before charge summing. The blue circles represent the amount of charge measured in each pixel. Right: after charge summing, the total charge is allocated to the pixel that measured the largest amount of charge, as represented by the blue circle.

spectroscopic imaging, in which materials associated with these lower energies have to be recognised.

1.2.2 Spectroscopic mode

Another mode that can be chosen to be implemented is the *spectroscopic mode*. In this mode, four pixels in a 2x2 square are connected to form one *superpixel*. The pixel-pitch is increased from 55 µm in the regular *fine-pitch mode* to 110 µm. Since each individual pixel has two counters and two discriminators, the superpixel now has eight of both. This means that in sequential read/write mode, eight energy thresholds can be set, thus 7 energy windows can be looked at. This allows for so called *colour* imaging, since using the different energy thresholds, different parts of the x-ray spectrum can be selected. Since materials vary in the x-ray energies they absorb, this provides a way of identifying materials using x-ray imaging. Because multiple energy regimes can be looked at with only one image capture, this strongly reduces the radiation dose on the patient.

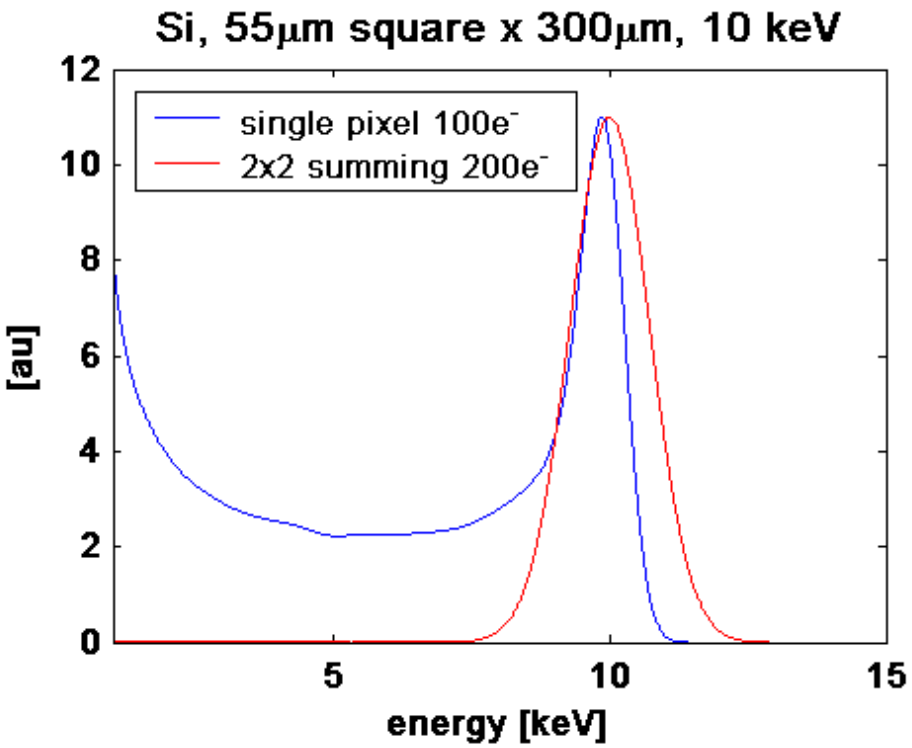

Figure 1.3 – The observed spectrum of a single pixeldetector of 55 µm exposed to photons of 10 keV using a 300 µm silicon sensor (in blue) compared to the simulated spectrum of a pixeldetector in the same conditions using charge summing (in red). [Absorbance in arbitrary units against the photon energy in keV. Image from Medipix collaboration CERN [2016].]

Chapter 2

Experimental setup

X-ray images of a test object that mimics features in the breast, microcalcifications (see section 1.1), have been made with the Medipix3RX and are analysed as described in section 4.1. The experimental setup is shown in figure 2.1.

2.1 X-ray source

A Hamamatsu L9421-02 Microfocus x-ray source has been used [Hamamatsu, 2011]. The reader is referred to appendix A.3 for a brief explanation of x-ray tubes. The device has a maximum tube voltage of 90 kVp which is plenty for the use in mammography, in which x-ray energies between 17 and 25 keV are preferred [Bushberg et al., 1994]. The x-rays are generated by an x-ray tube with a tungsten target and beryllium window of 150 µm. The latter is used in mammography to reduce the absorption of low energy x-rays [Bushberg et al., 1994]. The x-ray tube is operated at 25 kV, because this gave the best results for the phantom used in this research.

2.2 Test object

To determine the performance of the Medipix3RX detector, a contrast-detail (CD) phantom was used. The CDMAM-phantom 3.2 is specifically designed for the testing of mammography equipment and was made by St. Radboud University Nijmegen. The phantom can be seen in figure 2.2. It consists of a 0.5 mm aluminium plate that holds gold disks of varying thickness and diameter set in a grid. The entire plate is covered in a 5.5 mm PMMA[1] plate. The thickness of the gold disks increases exponentially from 0.05 µm to 1.60 µm while the diameter increases exponentially from 0.10 mm to 3.20 mm across a row and column, respectively. Within each row the diameter is constant while the thickness varies and vice versa within each column. Each square corresponding to a certain diameter and thickness[2] contains two identical disks. One is placed in the center of the square and the other is placed in a random corner, to prevent any patterns and expectation, since the phantom is often used in experiments where the visibility is tested by several human observers. See Suryanarayanan et al. [2007] and Suryanarayanan et al. [2002] for such experiments.

2.3 Medipix3RX

For this experiment a quad of Medipix3RX-based detectors was used, spanning an area of approximately 28×28 mm. As mentioned in section 1.2, the detectors consist of a silicon sensor that is bump bonded to the Medipix3RX ASIC[3]. The reader is referred

[1] Polymethylmethacrylate, also known as acrylic glass or by tradenames such as Plexiglas and Perspex.
[2] Such a square is hereafter called a *phantom square*.
[3] Application specific integrated circuit.

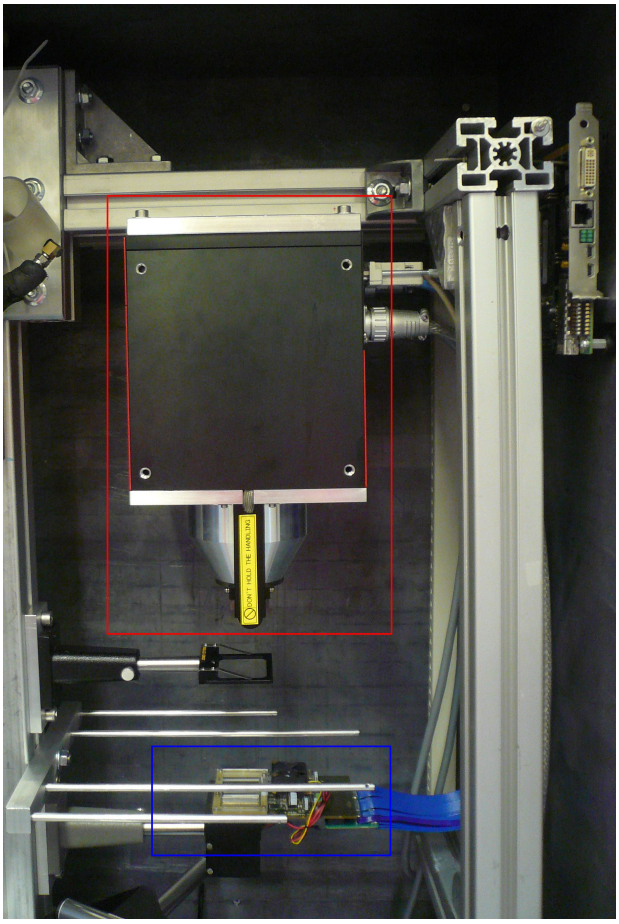

Figure 2.1 – The experimental setup that was used to make the x-ray images of the CDMAM phantom with the Medipix3RX detector. The X-ray source can be seen inside the red frame while the detector and its readout can be seen inside the blue frame and in the top right corner.

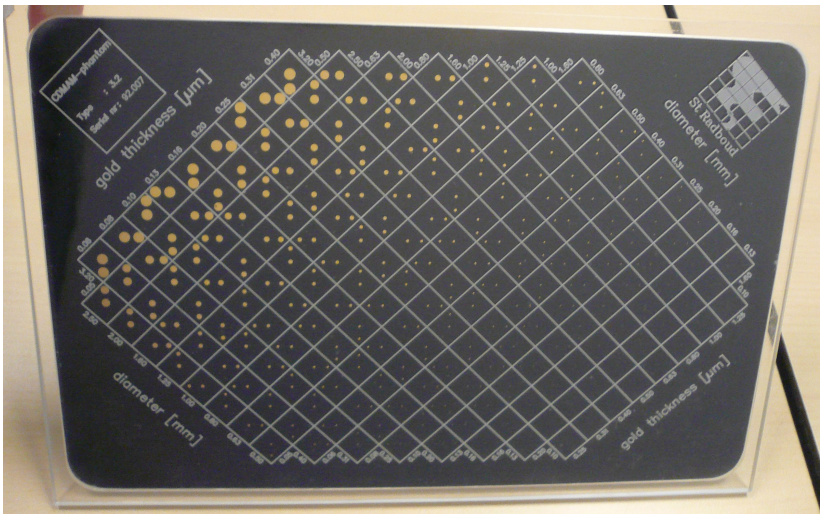

Figure 2.2 – A photo of the phantom that was used. The specks of gold vary in size and thickness and represent micorcalcifications.

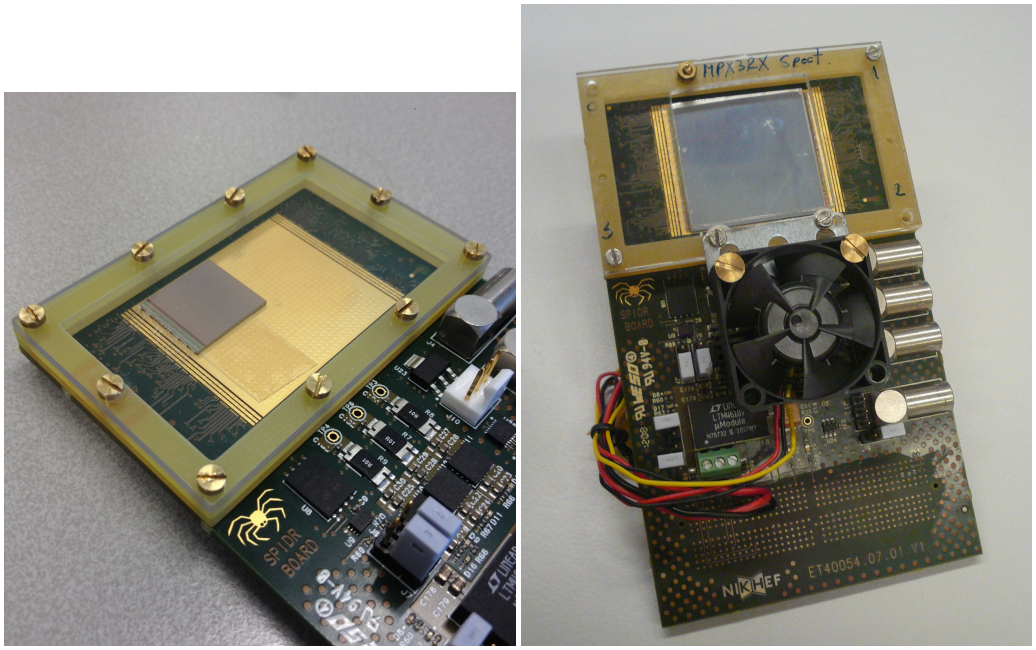

(a) A SPIDR board with one Medipix3RX chip installed. Image from Beuzekom [2016].

(b) The SPIDR board with four Medipix3RX chips and cooling fans installed.

Figure 2.3 – SPIDR boards

to appendix A.3 for more details on the detection of x-rays. Unfortunately, one of the four chips in the quad was already disfunctional. The Medipix3RX detectors were read out with a Speedy Pixel Detector Readout module (SPIDR) powered by an FPGA[4] that transports the data via UDP[5] to a computer using a 1Gb ethernet connection. The SPIDR board was developed by the Detector R&D department at Nikhef[6] to read out multiple Medipix detectors. The detector with its readout is depicted in figure 2.3. For more information, see the SPIDR twiki [Beuzekom, 2016].

2.4 Software

To analyse the data taken by the detector, software has been developed by the Detector R&D department of Nikhef. The graphic user interface (GUI) is shown in figure 2.4 and was developed at Nikhef. An earlier bachelor project, Deckers [2015], contributed to this as well. A heat map is shown to the left, indicating the photon count of each pixel. A histogram of these photon counts is presented to the right. Not only is the data collected and visualized by the GUI, it also allows the user to control the SPIDR board in an easy and straightforward way. The most important and relevant to this research are the options to take new data, integrate it over multiple frames (shutter openings) and switching between single pixel and chargesumming mode (see section 1.2.1). It has been developed in a cross-platform application framework, the so-called Qt (see The Qt Company [2016]). For more details about developement and funcionality of the Medipix3 GUI, see Deckers [2015]. The software has been extended in this research to better serve as an analysis tool for both a user and researcher. All additions to the software relevant to this research will be discussed in chapter 3.

[4] Field-programmable gate array.
[5] User Datagram Protocol.
[6] The National Institute for Subatomic Physics.

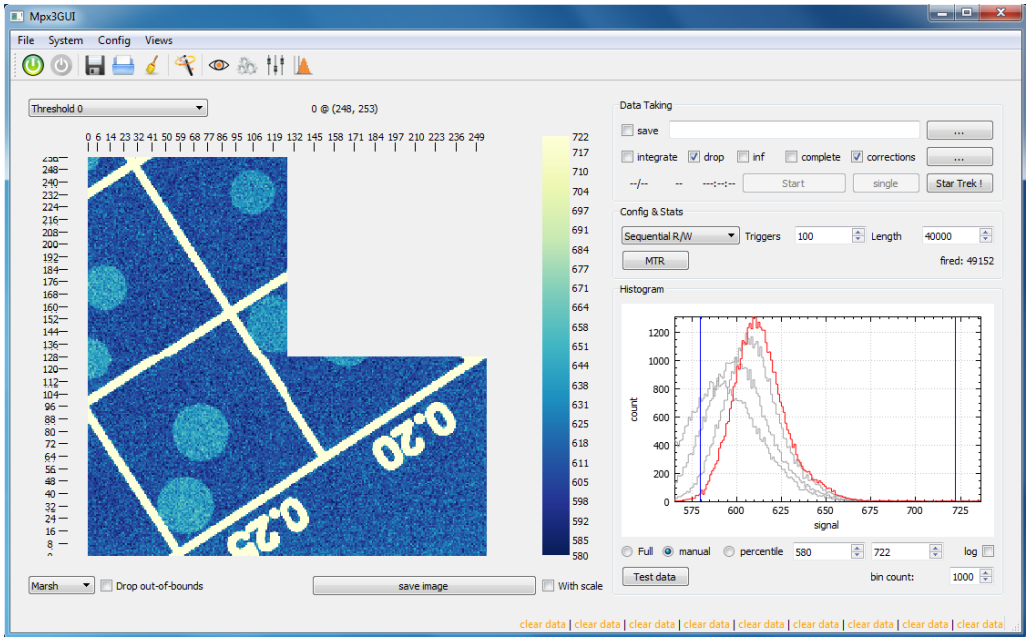

Figure 2.4 – Screenshot of the GUI as it was developed by the Detector R&D department at NIKHEF.

Chapter 3

Imaging analysis techniques

3.1 Corrections

The raw data collected by the detector, as seen in figure 3.1a, still shows features that are due to the pixel dependent response. For example, bright lines can be seen at the borders between chips. The reason for this is that these pixels have slightly larger area and thus collect more photons. Moreover, since each individual pixel has its own circuitry they have a different energy dependency and thus can give different signals at exactly the same incoming charge. To differentiate this from the actual differences in incoming signal due to the object that is measured, corrections have to be applied. Two such corrections are discussed in the following sections: the *open beam correction*[1] and the *beam hardening correction*. The latter yields a better image, as can be seen in figure 3.1, and has been applied in the analysis.

3.1.1 Open beam correction

By using an image made without any object in front of the detector (open beam) any artifacts caused by sources other than the object of interest will be filtered out. Photon attenuation for a homogeneous medium of thickness t is given by Beer's law

$$I = I_0 e^{-\mu t}, \tag{3.1.1}$$

in which I is the detected intensity, I_0 is the original intensity before it passed through the medium and μ is the photon absorption coefficient. This can be rewritten to

$$-\log(\frac{I}{I_0}) = \mu t. \tag{3.1.2}$$

By plotting the natural logarithm of the ratio of the signal I to the open beam signal I_0, instead of plotting the signal of the detector I, we have a direct link to the absorption coefficient [Schioppa, 2014].

3.1.2 Beam hardening correction

Beam hardening is the process in which the effective energy of an x-ray spectrum is shifted towards higher energy (harder x-rays) by absorption of lower energy photons. This occurs when taking an image of any object. When the x-ray beam goes through a layer of the object, the spectrum in the next layer is different (harder). This effect can be seen clearly in figure 3.2. When using x-rays with a continuous spectrum this effect has to be taken into account, since the attenuation coefficient depends on the energy of the incoming x-ray radiation [Bushberg et al., 1994].

[1] Also called a *flat-field correction.*

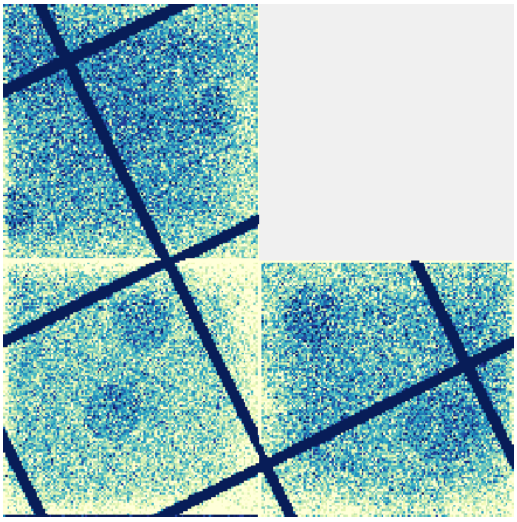

(a) Example of raw data taken by the Medipix3RX based detector.

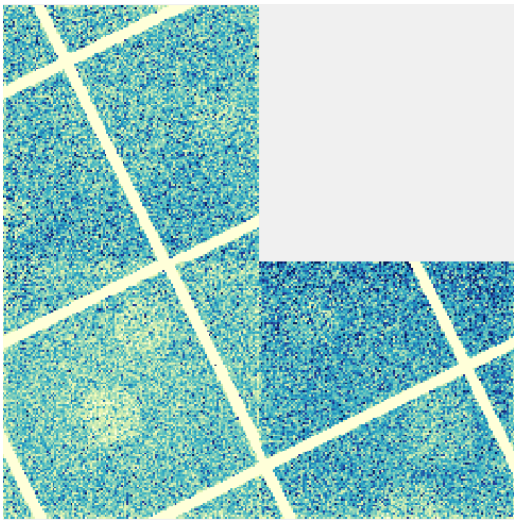

(b) The image after an open beam correction was applied.

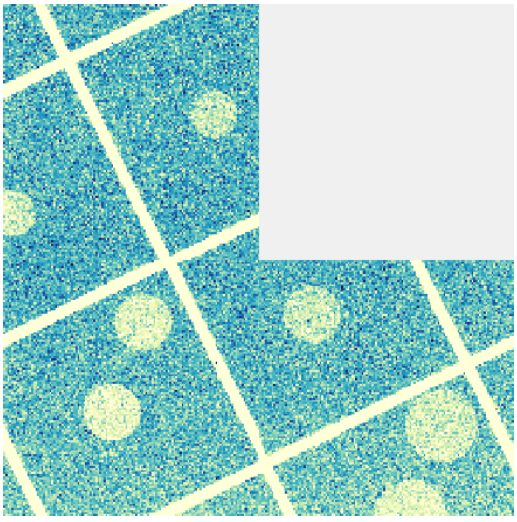

(c) The image after a beam hardening correction was applied.

Figure 3.1 – Corrections on raw data.

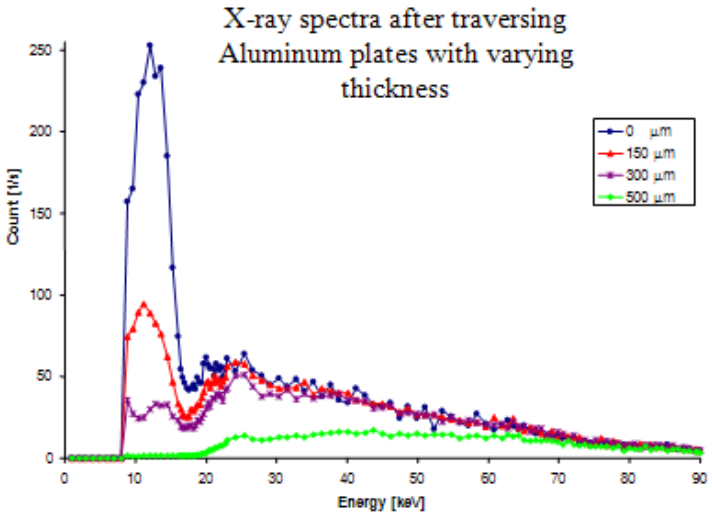

Figure 3.2 – Beam hardening caused by aluminium plates of varying thickness. Image from Kabůkek [2016].

The correction filters out artifacts caused by attenuation of the x-ray spectrum by a certain thickness of material. By correcting with different thicknesses of aluminium, artifacts can be removed from the image in thicker as well as thinner parts of the object. The beam hardening correction was already implemented in the software as described by Chatziantoniou [2016] and Kabůkek [2016] and was used as such. In short: multiple open beam images are made, each with a different aluminium filter, increasing in thickness. The measured signal of each pixel is then converted to a thickness by means of interpolation. This method is useful when regions of high and low attenuation appear in the same image.

3.2 Contrast-to-noise ratio

To assess the performance of the Medipi3RX-based detector it is needed to quantify how the human eye resolves a tested object. The so-called contrast-to-noise ratio (CNR) was used, defined by Bao and Chatziioannou [2010] as

$$CNR = \frac{S_l - S_{bg}}{\sigma_{bg}}\sqrt{n_l}, \tag{3.2.1}$$

in which S_l and S_{bg} are the signals of the lesion and background, respectively. The σ_{bg} is the standard deviation of the background and n_l is the number of pixels that the lesion occupies. According to Rose [1974] this CNR should exceed 5 to be visible.
To determine if a certain area contains a lesion which significantly stands out, a profile can be made of the area in both the x- and y-direction. An example is shown in figure 3.3. In this case, a profile in the horizontal direction was made, meaning all pixel values in a column above an x-value were added up and plotted. The same can be done in the vertical direction; all pixel values in a row would then be added and plotted. To calculate the CNR, (lesion)signal and background are needed. The user can select these by hand, choosing either one background or two backgrounds at either side of the signal. Alternatively, the user can choose to calculate the six points indicating the signal and two backgrounds using the kernel density function, described in the next section. See appendix B.3 for more details on the implementations made in this research project, such as all functionalities of the profiledialog.
When a profile has been made, the CNR can be calculated by selecting the region that is to be taken as the lesion and the region(s) that should be taken as the background. For S_l and S_{bg} the mean of the lesion and background regions are taken, respectively. The standard deviation of the background region(s) were taken for σ_{bg}. For n_l the number of columns or rows inside the indicated lesion region was taken.

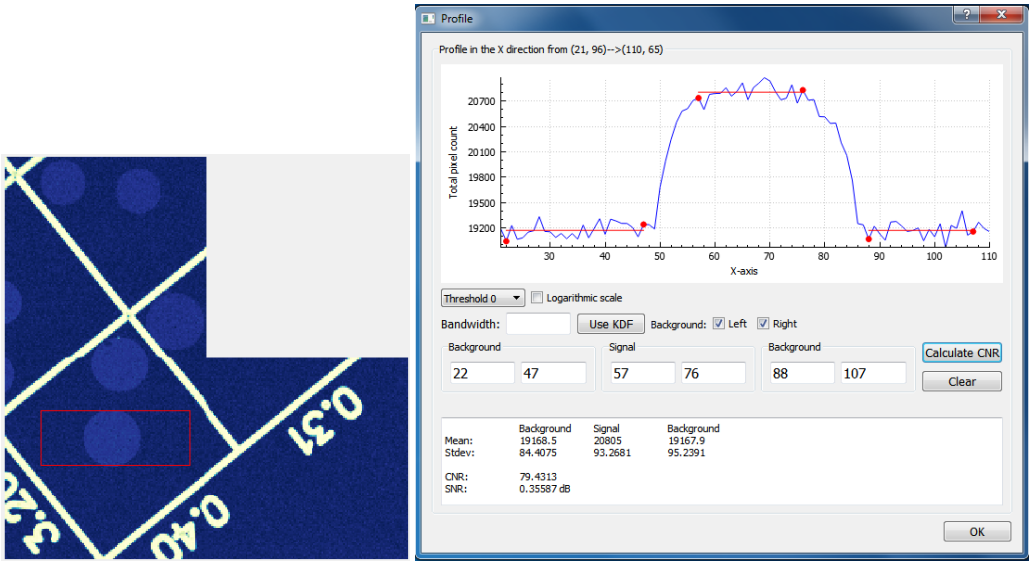

(a) Example image. **(b)** Profiledialog with CNR calculation.

Figure 3.3 – Example of the analysis of an image.

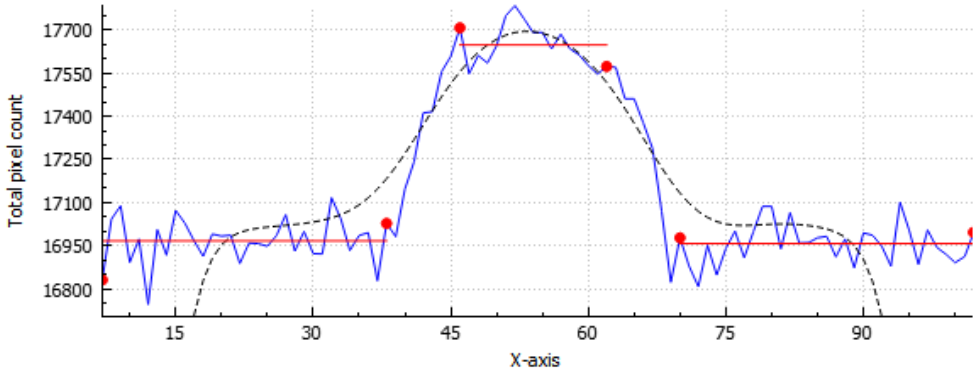

Figure 3.4 – Profileplot with kernel density function (black dotted line), boundary points (red dots) and mean values (red lines) indicated.

3.3 Kernel density function

When calculating the CNR, three regions need to be indicated by six points. A way of doing this automatically is with the kernel density function (KDF). Gaussian functions are created for each point along the profile, with a certain bandwidth that can be adjusted by the user. The kernel density function then adds up all the values of these gaussians at each point on the profile. This way a smoothed function is created, which follows the trend of the profile. The inflection points of this function can be determined by calculating the second derivative. Stepping some set distance[2] towards the maximum gives two points indicating the signal. Stepping the same distance outwards, indicates the boundary points of the background, excluding the step up. The kernel density function can be seen in figure 3.4, as well as the boundary points that are selected by performing the KDF procedure. Near the edges the KDF is seen to deviate quite a bit from the profile plot. This is caused by the lack of gaussian information near the edges. These parts are however not of interest when determining the boundary points for the CNR calculation, since the outer edges are always the first and last boundary points.

[2] In this research project, $\frac{1}{3}$ of the distance from the inflection points to the maximum has been chosen.

Chapter 4

Phantom characterisation

The phantom, as described in section 2.2, has been characterised in terms of visibility, expressed in the contrast-to-noise ratio, as described in section 3.2. The characterisation of the Medipix3RX-based detector will be compared to a characterisation using clinical data later this year. The method of analysing the data taken by the detector shall be described, followed by the results of this preliminary characterisation.

4.1 Method

The kernel density function for determining the boundary points was used on each image with a gaussian bandwidth of 5 pixels. The CNR was calculated with those points. To make sure the KDF could be properly used, a region was selected that contained sufficient background on both sides of the lesion signal (see section 3.3). This meant only the disks in the middle of each square could be used. The x- or y-direction of the profile was chosen based on the position of the other disk. If both were possible, both were taken into consideration. The procedure to calculate the CNR was repeated five times for each disk, of which the mean and sample standard deviation were taken and presented in section 4.2. If the points calculated by the KDF were too significantly off, they were adjusted by hand. If the KDF could not determine the boundary points with a bandwidth of 5 pixels, a larger bandwidth was used (6 pixels was usually sufficient).
To reduce the influence of time dependence (see discussion), a beam hardening correction has been made every one or two hours and used on the corresponding images. Dead pixels (three in total) have been set to the average of the surrounding pixels, to prevent the zero-values from increasing the background noise unnecessarily.
All phantom squares were positioned in the bottom left chip of the Medipix3RX-based detector (see section 2.3) to prevent any effects from differences between chips affecting the results. Before analysing an image, a beam hardening correction was applied, since the object contains regions of high attenuation (the line pattern) as well as regions of low attenuation contrast (the gold disks on aluminium).

4.2 Results

The results of the analysis of the data can be found in table 4.1, where the CNR values of each phantom square of the calibration phantom is reported. Cases in which no proper boundary points could be determined by the kernel density function are indicated with an x. CNR values below the Rose criterion are marked in red. In figure 4.2 a line is drawn below which these CNR values lie. This line thus represents the boundary of visibility of the disks. In figure 4.1 a comparison is shown for a few values of the CNR, in particular three close to the Rose criterion of 5 and one that is well above. From this comparison we can see that the CNR agrees quite well with what we can see. Figure 4.1a shows a disk that is not quite visible and is below the Rose criterion. Figure 4.1b lies on the border of the Rose criterion (taking the error into account) and is just distinguishable. Figure 4.1c

shows an object with CNR above the Rose criterion and is more easily discernable than the object in figure 4.1b, since the photon count density is significantly higher than that of the background. The second disk in this image can be located more easily as well. Finally, figure 4.1d shows an object of high contrast that is easily distuingished from the background and (thus) has a very high CNR.
The CNR reported in table 4.1 increase within a row as the thickness increases and decrease within a column as the diameter decreases. This is as expected, since the attenuation of a disk increases with the thickness and the visibility increases with diameter as more pixels make up the signal and stand out from the background.
The CNR value for (1,25; 0,25) is slightly too high to fit into this pattern but agrees within one sigma. The value for (1,25; 0,20) however stands out more and barely agrees with the value of (1,00; 0,20) within two sigmas. This could be due to a slight difference in analysis, see discussion. The pattern is also disrupted at the disks of small diameter, when below the Rose criterion. Since they are not visible, it is harder to analyse them objectively (see discussion). The values of these smaller disks below the Rose criterion of 5 thus don't really mean anything. The pattern is restored as soon as values get above the Rose criterion.
Negative CNR values occur when the KDF could only allocate a signal that was below the background. Since the absolute values are never above the Rose criterion, these negative signals are just noise fluctuations. Similar to this are the cases in which the KDF was not able to detect a signal at all, even after trying various bandwidths, denoted by an x in the table. Obviously this means the disk is not visible.
In the bottom right corner of the table the pattern is disrupted. The source of this is the charge sharing that occurs between pixels, as described in section 1.2.1. Since these disks are only about two pixels in size, the stochastic variability that the charge sharing introduces is more important.
The disks above the red line in figure 4.2 are the ones that can be seen using the Medipix3RX-based detector.

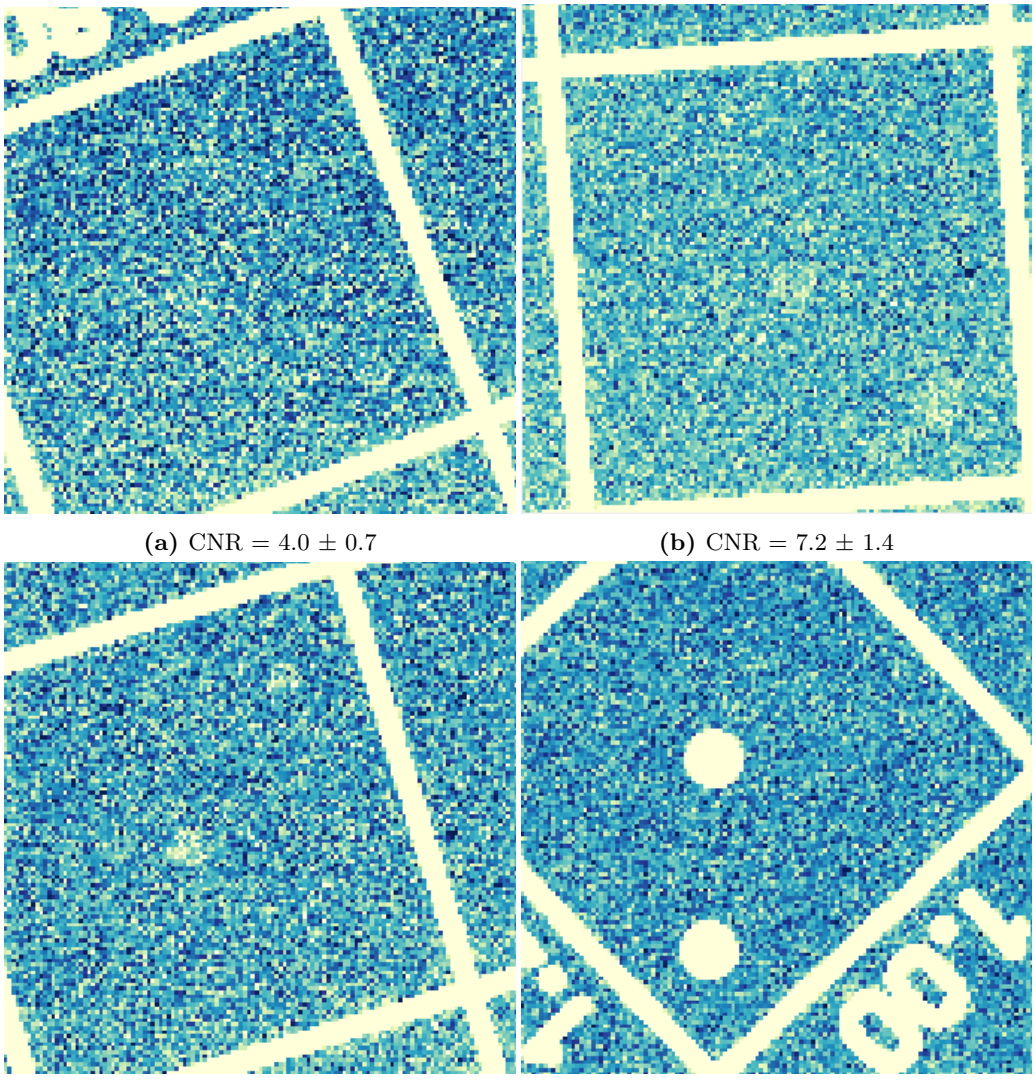

(a) CNR = 4.0 ± 0.7 **(b)** CNR = 7.2 ± 1.4

(c) CNR = 9.1 ± 0.3 **(d)** CNR = 108 ± 14

Figure 4.1 – Three different images with CNR just below, just above and well above the Rose criterion. Images were cut to show only the the bottom left chip. Zoomed in on approximately the same part of the photon counting histograms. The diameter and thickness of each imaged disk: (a) 0.80 mm, 0.05 µm (b) 1.00 mm, 0.08 µm (c) 0.80 mm, 0.10 µm (d) 1.25 mm, 1.00 µm.

Table 4.1 – Contrast-to-noise ratios for all disks on the CDMAM 3.2 phantom.

	t (µm)							
d (mm)	**0,05**	**0,06**	**0,08**	**0,10**	**0,13**	**0,16**	**0,20**	**0,25**
3,2	-	14,3±1,0	19,4±1,5	24,4±0,4	33,3±2,5	39,3±0,9	40,5±1,5	61±4
2,5	5,8±0,4	7±2	14,4±1,1	22,3±0,7	26,9±1,5	3,2±0,9	42,0±2,6	45,4±1,2
2	5,8±0,4	8,5±0,8	9,7±0,6	16±3	18,4±0,9	21,1±0,7	26,0±2,3	42±3
1,6	5,9±0,3	5,5±0,3	9,8±0,8	12,2±0,9	15,9±1,3	21,7±1,3	24,9±1,4	28,4±1,7
1,25	4,81±0,36	7,5±0,5	11,2±0,8	13,1±0,8	12,3±0,3	17,1±0,8	28,9±0,7	30±2
1	4,8±1,2	5,9±0,9	7,2±1,4	9,2±0,4	12,3±1,4	17,5±2,6	19,5±0,9	24,5±1,3
0,8	4,0±0,7	2,7±1,5	5,0±0,6	9,1±0,3	8,6±0,7	11,9±0,7	15±1	31±2
0,63	2,0±0,1	1±2	2,8±2,6	4,7±0,6	7,3±0,4	8,6±0,8	11,6±0,9	11,5±1,2
0,5	x	0,7±1,2	3,0±1,4	2,8±0,4	6,9±0,7	5,6±0,8	10,6±0,8	11,0±0,8
0,4	-	2,5±0,5	0±2	2,6±0,5	5,4±0,6	5,6±0,7	6,3±0,8	9±2
0,31	-	-	0,5±0,9	0,8±0,9	-0,4±1,7	3,3±0,7	6,2±0,9	7,3±0,3
0,25	-	-	-	-0,4±0,9	2,6±0,3	1,2±0,4	4,93±0,18	4±1
0,2	-	-	-	-	1,1±0,3	2,2±0,6	-0,5±1,5	4,6±0,5
0,16	-	-	-	-	-	2,7±1,7	-0,5±1,6	3,7±0,9
0,13	-	-	-	-	-	-	1,8±0,2	0±1
0,1	-	-	-	-	-	-	-	1,2±0,7

	t (µm)							
d (mm)	**0,31**	**0,40**	**0,50**	**0,63**	**0,80**	**1,00**	**1,25**	**1,60**
3,2	68,7±1,6	101,6±1,1	-	-	-	-	-	-
2,5	56,6±1,5	92±4	99±4	-	-	-	-	-
2	49,2±1,2	57±2	72,2±1,3	100±3	-	-	-	-
1,6	44,2±2,4	52±3	73±3	89±2	106±3	-	-	-
1,25	34,7±3,2	51±6	57±3	75,8±1,5	94±6	108±14	-	-
1	32±2	38±4	49,1±1,6	62±5	72±9	97±7	102±18	-
0,8	25,8±1,7	30±3	35,1±1,6	46±2	53±1	77±3	92±13	110±13
0,63	16,1±2,5	29±3	32,3±1,2	40,5±1,8	44,1±2,6	58±1	75±3	89±14
0,5	16,1±1,4	18,5±1,7	26,1±0,9	32,0±2,4	41±2	49±6	60±10	70±9
0,4	10,9±0,3	14,3±0,7	18±1	20±2	29±2	34,5±1,5	39±3	49,1±1,8
0,31	9,1±0,4	11,8±0,7	17±2	17,8±0,9	21±4	8,30±0,26	34±4	45±3
0,25	4,76±0,36	9,7±1,6	11,6±0,2	14±1	17,8±0,9	23±1	24,9±2,4	29±4
0,2	3,6±0,8	6,62±0,13	8,39±0,18	12,1±1,2	12,1±1,2	13,3±0,4	20,6±1,8	22,4 ±1,4
0,16	-0,5±0,6	4,5±0,3	4,46±0,05	7,9±0,3	8,8±0,5	11,5±1,2	12,5±0,9	14±1
0,13	1,9±1,8	3,1±0,5	1,9±1,5	5,3±0,4	4,6±0,5	6,7±0,5	4,9±1,2	11,8±0,2
0,1	-2,2±0,9	x	3,5 ±0,5	4,2±0,8	3,85±0,16	5,5±0,6	7,8±1,4	-

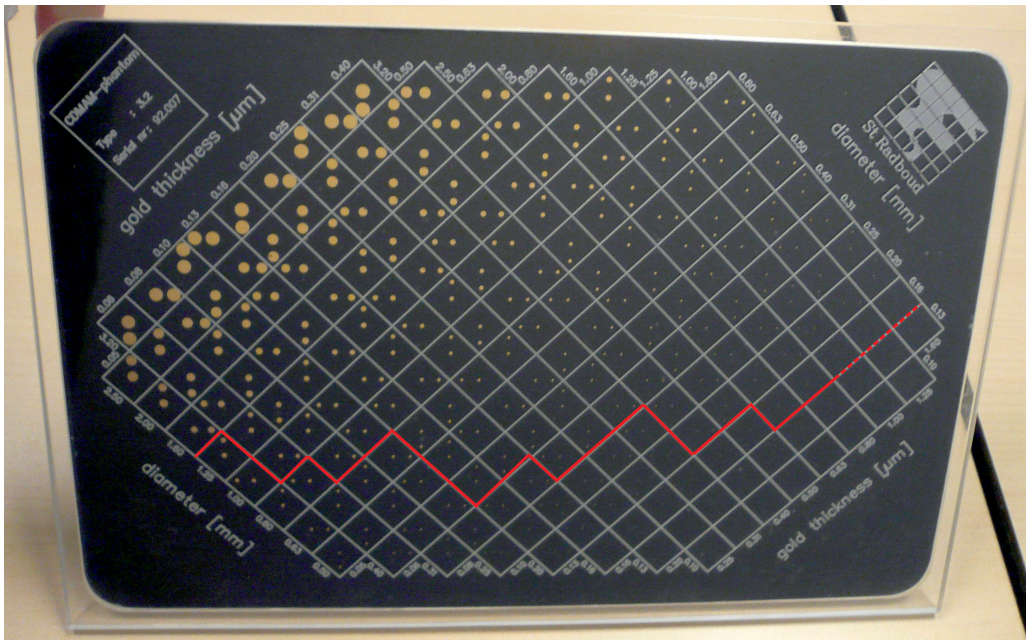

Figure 4.2 – The CDMAM 3.2 calibration phantom. The red line indicates the boundary of the Rose criterion.

Chapter 5

Conclusion

The software developed in this research project has proven to be useful in the analysis of x-ray images taken with the Medipix3RX detector. By creating a profile of a selected region, the variability between pixels is shown to the user. Specifically, the software is able to quantify the visibility of a signal with respect to the background by means of the contrast-to-noise ratio. This CNR was shown to be in agreement with expectations for signals that are significantly larger than the pixel pitch[1]. For these signals, the implemented kernel density function procedure is capable of selecting the signal boundary points automatically, making data analysis easier and faster for the user and more independent of the user's sight and skill.

5.1 Discussion

When taking the first measurements and applying different beam hardening corrections, differences were noticed between images and corrections taken at different times. A strong time dependence caused an image taken in the morning to have a lower CNR than one taken in the afternoon, even when corrected with beam hardening corrections taken at the corresponding times. The Medipix3RX-based detector version that was used has been known to have issues, in particular with leakage current. Due to time constraints it was not possible to work with a newer version yet. To reduce the effect of time dependence, measurements were taken only in the afternoon, after the Medipix3RX based detector, SPIDR readout board and bias current had been running for at least four hours. Beam hardening corrections were made every one or two hours and images were corrected with the correction that was made closest to that measurement. Because of the large amount of data that had to be taken and analysed, both had to be done over several days. Since the energy dependence of the equipment and analysis skill varies over time, the results presented in section 4.2 should be seen as a first indication of the performance of the CNR and KDF implementations. A more controlled experiment is needed for a more precise characterisation of a certain setup and phantom.
Due to the limitations of the KDF (see appendix B.3) only the disks in the center of each phantom square were evaluated. This of course introduced a bias in the region selection of barely visible disks. However, this research project does not focus on the identification of lesions by test subjects, but on the characterisation of each of the gold disks on the plate. For this it is needed to correctly choose a region even when the object of interest is not visible to the human eye, since for these objects the CNR was to be calculated as well. Were the software to be used in an identification research, the KDF must be improved to work for two regions[2], to be able to calculate the CNR using the KDF near the edges of a phantom square as well. Alternatively, the CNR can be calculated by choosing the boundary points by hand. This has not been done in this research to maintain a certain standard for each signal identification and reduce bias. However, the two signal boundary points have been adjusted when it was obvious that the KDF

[1] The width of a pixel, i.e. the distance between pixels, in this case 110 µm.
[2] The two regions being the signal and the background on one side of the signal.

calculation did not locate these appropriately. This was specifically the case for the gold disks of smaller diameter. When the signal is only a few pixels wide, the distance from an inflection point to the maximum is also only a few pixels and gets below 3 pixels at some point. Since the program uses the discrete pixels as boundary points and takes $\frac{1}{3}$ of the mentioned *integer* distance, at some point the step away from the inflection point[3] becomes zero. An example of such an occurence is shown in figure 5.2, where gold disks with a diameter of 0.13 mm and a thickness of 1.00 µm are imaged. Since the pixels of the detector are 110 µm wide and there is some magnification, these points take up two pixels at most. When knowing which pixels to select, as is the case with the disk in the middle, a profile as seen in 5.2c can be created, in which a peak can clearly be seen and a CNR above the Rose criterion is calculated. Looking at figure 5.2a however, the second disk is not so easily located.

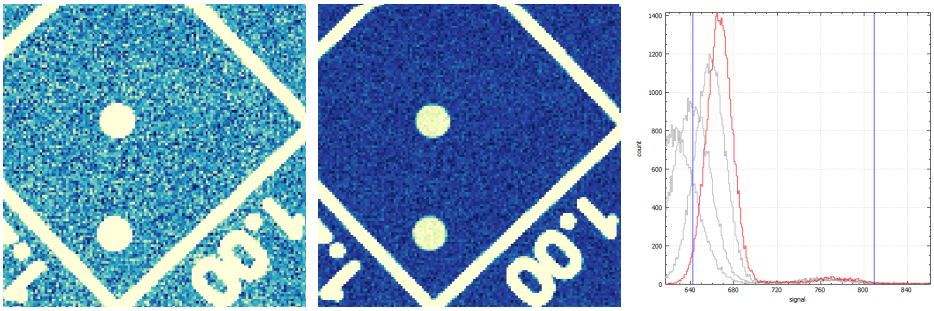

(a) CNR=108±14, zoomed in on the left peak of the pixel-count histogram.

(b) CNR=108±14, corresponding to the histogram shown in figure c.

(c) Image of gold disks of 1.25 mm in diameter and 1.00 µm thickness at different parts of the pixel-count histogram.

Figure 5.1 – Image of gold disks of 1.25 mm in diameter and 1.00 µm thickness at different parts of the pixel-count histogram.

Concerning location of the disks, when creating a profile of the thinner, less visible disks, a larger region had te be chosen to be sure the disk would be contained. This however means some noise is added to the columns (or rows) containing the signal, lowering the total column signal and thus the CNR. This ultimately means the less visible and harder to locate objects are biased to get a lower CNR, while more easily dicernable objects are biased towards higher CNR. The latter is because these objects also have a much clearer profile, of which the boundary points are quite clear. The points decided on by the KDF can be adjusted to these obvious choices, raising the CNR. While for the less visible objects the profile boundary points are not so easily seen and thus the KDF points are used.
It can also be questioned if the Rose criterion for the visibility of a signal is valid in this case. In Rose [1974] the boundary for visibility is chosen at a threshold signal-to-noise ratio of 5. This is based on a spatial distribution of noise and signal, while in this research project the contrast-to-noise ratio of the profile was calculated. Like the examples shown in figure 4.1, objects that had a CNR below the Rose criterion in this preliminary analysis were not visible to the eye, while the objects with CNR significantly above the Rose criterion can be identified by the human eye [4]. What the CNR calculation does not take into account however, is the dependency of the human eye to colour contrast. When comparing figures 5.1a and 5.1b or 5.2a and 5.2b, it is clear that plotting a different part of the pixel-count histogram, thus changing the range in colour and contrast can result in better contrast, which is normal practice. When calculating the CNR however, the absolute values of each pixel are used. So in fact the CNR does not represent the visibility of what is shown on the user's computer screen.

[3] See section 3.3 for an explanation of the KDF procedure.
[4] More importantly perhaps; the second disk can also be located.

Nevertheless, the CNR calculation in the software provides a way to compare data taken by seperate setups.

5.2 Outlook

To complete the software developed in this research project, the improvements and extensions mentioned in appendix B.3 should be implemented. In addition, to make sure the kernel density function identifies appropriate boundary points even in the case of a spatially small signal as mentioned above, the step in from the inflection points should be changed. The use of integer pixels and their values is limiting in these smaller regimes. Interpolation or fitting of the profile could be applied.
The next step in the development of the Medipix3RX-based detector would be to do a similar contrast-to-noise analysis in charge summing mode. This mode should provide much better resolution. Blurring around the edges of lesions due to charge sharing among pixels would be eliminated, thus increasing the CNR. This would also resolve the inconsistency of the CNR of small diameters seen in table 4.1. The full capabilities of spectroscopic mode should also be explored. The use of multiple thresholds can be shown qualitatively for material recognition[5] but should be shown quantitatively in the context of medical imaging. Before that, the calibration phantom used should be characterised by hospital equipment for a direct comparison of the current performance. But first of all, dosimetric measurements will be done, to ensure the goal of the Medipix3RX based detector, which is to detect microcalcifications with lower doses to the patient.

[5] The capability of distinguishing different overlapping metal foils has been shown by Ballabriga et al. [2013].

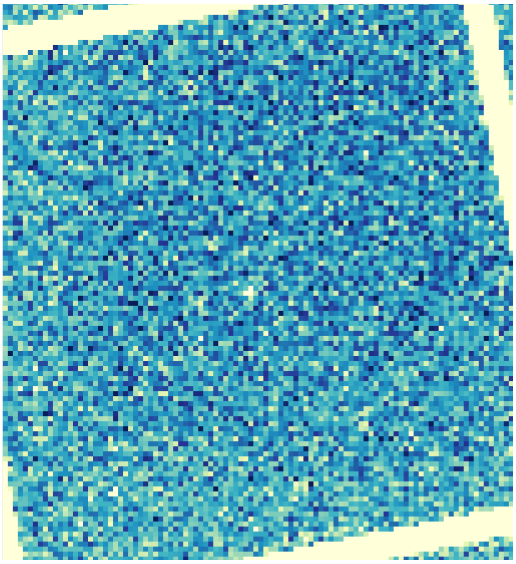

(a) CNR = 6.7±0.5

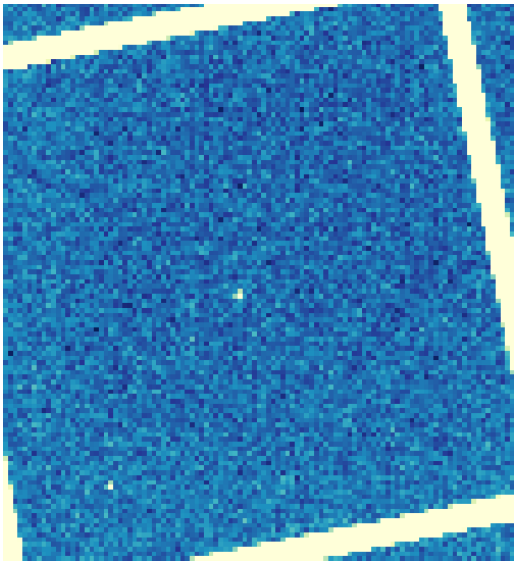

(b) CNR = 6.7±0.5, zoomed out.

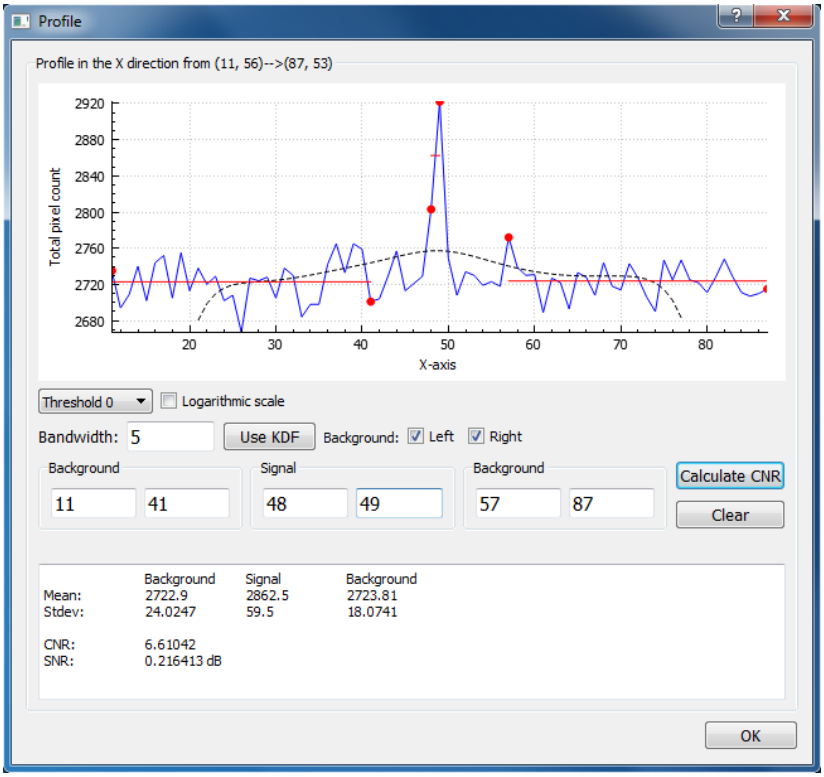

(c) One of the profiles taken of the center disk. The signal boundary points were adjusted. See appendix B.2 for details on the dialog.

Figure 5.2 – Image of gold disks of 0.13 mm in diameter and 1.00 µm thickness, at different parts of the pixel-count histogram.

Bibliography

Ballabriga, R., Alozy, J., Blaj, G., Campbell, M., Fiederle, M., Frojdh, E., Heijne, E. H. M., Llopart, X., Pichotka, M., Procz, S., Tlustos, L., and Wong, W. (2013). The medipix3rx: a high resolution, zero dead-time pixel detector readout chip allowing spectroscopic imaging. *Journal of Instrumentation*, 8(02):C02016.

Ballabriga, R., Campbell, M., Heijne, E., and Llopart, X. (2011). Medipix3: A 64k pixel detector readout chip working in single photon counting mode with improved spectrometric performance. *Nuclear Instruments and Methods in Physics Research Section A: Accelerators, Spectrometers, Detectors and Associated Equipment*, 633(supplement 1):S15 – S18.

Bao, Q. and Chatziioannou, A. F. (2010). Estimation of the minimum detectable activity of preclinical pet imaging systems with an analytical method. *Medical Physics*, 37(11):6070–6083.

Beutel, J., Kundel, H. L., and van Metter, R. L. (2000). *Handbook of Medical Imaging, Volume 1: Physics and Psychophysics*. SPIE: Society of Photo-Optical Instrumentation Engineers.

Beuzekom, M. v. (2016). Spidr twiki. http://wiki.nikhef.nl/detector/Main/SpiDr.

Bushberg, J. T., Seibert, J. A., Jr., E. M. L., and Boone, J. M. (1994). *The Essential Physics of Medical Imaging*. Williams and Wilkins.

Chatziantoniou, C. (2016). Beam hardening correction in multi-spectral mammography. Bachelor thesis, Utrecht University.

Deckers, R. G. A. (2015). Multi-spectral mammography using a medipix3rx based detector. Bachelor thesis, Utrecht University.

Durini, D. (2014). *High Performance Silicon Imaging: Fundamentals and Applications of CMOS and CCD Image Sensors. Chapter 2*. Woodhead Publishing.

Hamamatsu (2011). *90 kV Microfocus X-ray Source L9421-02 Instruction Manual*. Hamamatsu Photonics K. K., 314-5 Shimokanzo, Iwata City, Shizuoka Pref., 438-0193, Japan. Ver. 1.4.

Kabůkek, J. (2016). Beam hardening correction. Czech Technical University.

Karsa, L. v., Anttila, A., Ronco, G., Ponti, A., Arbyn, M., Segnan, N., Malila, N., Castillo-Beltran, M., Boniol, M., Ferlay, J., Hery, C., Sauvaget, C., Voti, L., and Autier, P. (2008). *Cancer Screening in the European Union: Report on the Implementation of the Council Recommendation on Cancer Screening, First Report*. European communities. International Agency for Research on Cancer.

Medipix collaboration CERN (2016). What is medipix3? https://medipix.web.cern.ch/medipix/pages/medipix3.php.

Nalawade, Y. (2009). Evaluation of Breast Calcifications. *Indian Journal of Radiology and Imaging*, 19(4):282–286.

Naseem, M., Murray, J., Hilton, J. F., Karamchandani, J., Muradali, D., Faragalla, H., Polenz, C., Han, D., Bell, D. C., and Brezden-Masley, C. (2015). Mammographic microcalcifications and breast cancer tumorigenesis: a radiologic-pathologic analysis. *BMC Cancer*, 15(1):1–9.

Prince, J. L. and Links, J. M. (2006). *Medical Imaging: Signals and Systems*. Pearson Prentice Hall.

Rose, A. (1974). *Vision: Human and Electronic*. Plenum Press.

Schioppa, E. (2014). *The Color of X-rays: Spectral X-ray Computed Tomography using Energysensitive Pixel Detectors*. PhD thesis, Universiteit van Amsterdam, 's Hertogenbosch.

Shetty, M. K. (2015). *Breast Cancer Screening and Diagnosis*. Springer New York.

Sternbach, G. and Varon, J. (1993). Wilhelm konrad roentgen: A new kind of rays. *The Journal of Emergency Medicine*, pages 743–745.

Suryanarayanan, S., Karellas, A., Vedantham, S., Sechopoulos, I., and D'Orsi, C. J. (2007). Detection of simulated microcalcifications in a phantom with digital mammography: Effect of pixel size. *Radiology*, 244(1):130–137.

Suryanarayanan, S., Karellas, A., Vedantham, S., Ved, H., Baker, S. P., and D'Orsi, C. J. (2002). Flat-panel digital mammography system: Contrast-detail comparison between screen-film radiographs and hard-copy images. *Radiology*, 225(3):801–807. PMID: 12461264.

The Council of the European Union (2003). Council recommendation of 2 december 2003 on cancer screening. *Official Journal of the European Union*, 11(6):34 – 38.

The Qt Company (2016). Qt homepage. https://www.qt.io/.

Appendix A

X-ray imaging

X-ray imaging has been around since 1895, when Wilhelm Conrad Roentgen experimented with a forerunner of an x-ray tube, discovering a new kind of rays. Not long after he published a radiograph of his wife's hand and only two months later x-rays were used clinically [Sternbach and Varon, 1993]. The ability to look inside solid objects without opening them has lead X-rays to be used in various applications.

A.1 Production of x-rays

X-rays are a kind of electromagnetic radiation with energies ranging (roughly) from 100 eV to 1000 keV and wavelengths in the order of nanometers. These energies are high enough to remove bound electrons from atomic shells, resulting in ionized atoms. X-ray radiation is therefore called ionizing radiation, along with ultraviolet radiation and gamma rays. In medical imaging an x-ray tube is used to produce this ionizing radiation. Such a device consists of an electron source and a metal target, often made of tungsten or molybdeen. A symplified x-ray tube diagram is shown in figure A.1. Electrons are supplied by the cathode to collide with the target material on the anode. The rest of the anode is often made of a different material that allows better heat transport. The window through which the electrons exit the x-ray tube can be made of different material to filter the x-ray spectrum.

The spectrum produced by an x-ray tube consists of two kinds of radiation: *bremsstrahlung* and *characteristic x-rays*. The first is produced when an electron interacts with an atomic nucleus. The electron is deflected by the electric field of the positively charged nucleus, resulting in loss of kinetic energy. This energy is emitted in the form of electromagnetic radiation, called *bremsstrahlung*[1]. The energy of the x-rays that are produced this way depends on the distance between the electron and the nucleus, as the electric field is larger near the nucleus. When an electron hits the nucleus head on, it loses all its kinetic energy. This process produces the largest possible x-ray energy, which is dependent on the incoming electrons. If an x-ray tube uses 90 keV electrons, the maximal photon energy is 90 keV. Since the probability of this happening is very low, this takes up a small part of the spectrum. Electrons deflected further from the nucleus occur far more often, but produce low energy photons. The resulting bremsstrahlung spectrum is depicted in figure A.2 as well as the filtered spectrum in which lower energy photons are absorbed by the x-ray tube housing. The most probable x-ray energies lie around $\frac{1}{3}$ to $\frac{1}{2}$ of the maximal photon energy in the spectrum. See Bushberg et al. [1994]. When the energy of the incoming electrons exceeds the binding energies of the inner shell electrons of the target material, characteristic x-rays can be produced. When such an electron interacts with an inner shell electron, i.e. an electron from the K- or L-shell, the latter can be ejected from its orbit. An electron from a higher shell will fill the vacancy. Because it goes to a shell of lower energy, it releases an x-ray photon with energy equal to the difference between the shells. Because shell energies are unique to a certain element,

[1] A German word referring to the fact that the electron is decelerated.

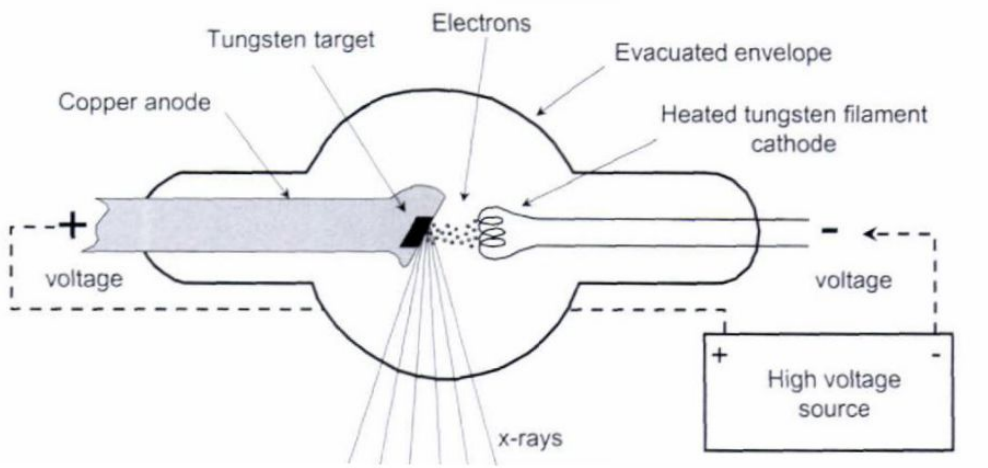

Figure A.1 – X-ray production requirements include a source and target of electrons, evacuated envelope, and high-voltage source. Reprinted from Bushberg et al. [1994, p. 66].

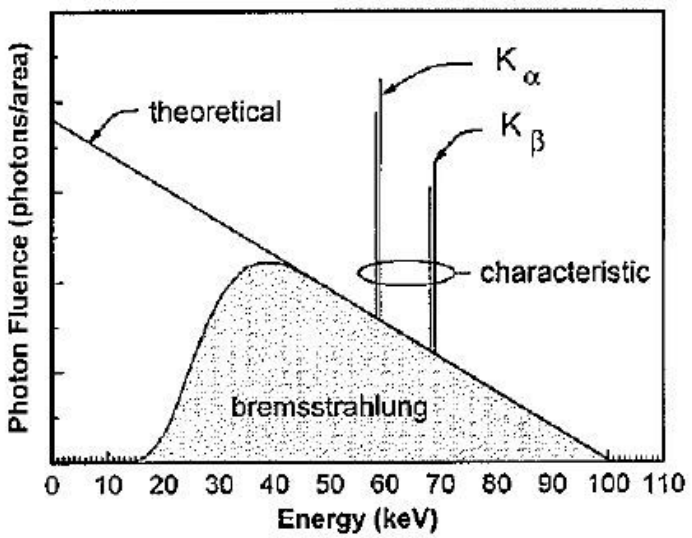

Figure A.2 – Idealized x-ray spectra are shown for 100 keV electrons striking a tungsten anode. The triangle-shaped theoretical spectrum produced inside the x-ray tube is attenuated by metallic structures in the tube, producing the shaded bremsstrahlung spectrum illustrated. Characteristic x-rays appear on the spectrum as line spectra. The doublets for K_α and K_β beta characteristic x-rays are illustrated. Reprinted from Beutel et al. [2000].

these x-rays are called *characteristic x-rays*. These photons create discrete energy peaks in the x-ray spectrum, on top of the continuous bremsstrahlung spectrum.

A.2 Absorption of x-rays

X-rays interact with matter in a few ways. The three most important processes are depicted and explained in figure A.3, which was taken from [Beutel et al., 2000]. The reader is referred to this book for an in-depth discussion of x-ray interactions.

A.3 Detection of x-rays

In figure A.4 we see that in the energy range of x-rays produced by x-ray tubes (about 20 keV to 150 keV) the photoelectric effect is dominant. This means the signal produced by a photon is proportional to its original energy. One can thus detect x-rays by making the photons deposit their energy in some material, a sensor, and convert this energy to a measurable signal. The very first application used a photographic plate which x-rays would directly expose by interacting with the chemical emulsion present on the film. But since only 1 to 2 percent of the x-rays are stopped by the film, creating a decent picture would require a high radiation dose on the patient [Prince and Links, 2006]. To increase the efficiency, intensifying screens using luminescent material are used. These screens convert the x-rays into light which then exposes the film much more effectively. Because of the conversion to light, these kind of detectors are called *indirect detectors*.
Nowadays, far more often *direct* solid-state detectors, such as the flat-panel detector, are used. In these detectors x-rays are directly converted into charge in a sensor layer that is made of a solid material that acts as an insulator when no x-rays are present. Selenium is often used as such a so-called photoconductor. Incoming x-ray photons create electron-hole pairs in the selenium by means of the photoelectric effect. These are guided to the detector by an electric field that has been set over the sensor. The detector then measures the total accumulated charge electronically [Beutel et al., 2000]. These detectors are so-called *energy integrating systems*, since they measure the total energy released by all photons that interacted with the sensor during the exposure.
New technology has led to the emergence of *active pixel devices* (such as the Medipix) in which each pixel has its own electronic circuitry, [Schioppa, 2014]. This allows each pixel to perform operations on the incoming charge, of which energy discrimination is most important. Only when an incoming charge is above a certain threshold (representing a minimal photon energy) will the counter of a pixel increase. The detector is thus a *photon counting detector* instead of an energy integrating system. On top of the chip containing all the pixel circuitry is still a semiconductor sensor, often silicon.

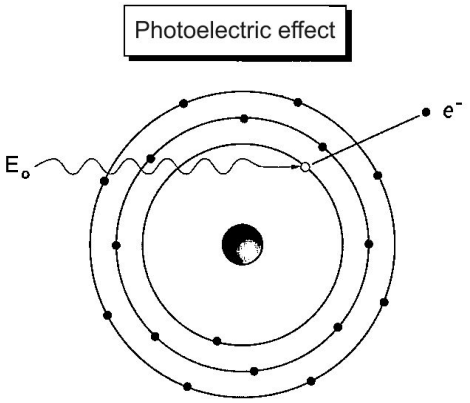

(a) In the photoelectric effect, an x-ray with energy E_0 is absorbed by an atomic electron, which is ejected from the atom causing ionization. The photoelectron will have kinetic energy equal to $E_0 - E_{BE}$, where E_{BE} is the binding energy of the electron to the nucleus.

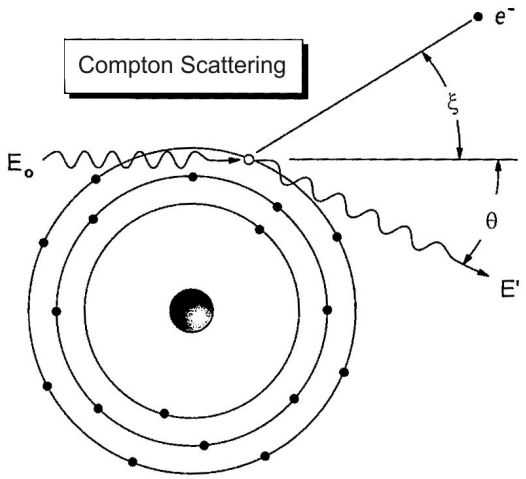

(b) In Compton scattering, an incident x-ray with energy E_0 interacts with an outer-shell electron. The electron is ejected from the atom, causing ionization. A scattered x-ray photon with energy E' emerges at an angle θ relative to the incident photon's trajectory.

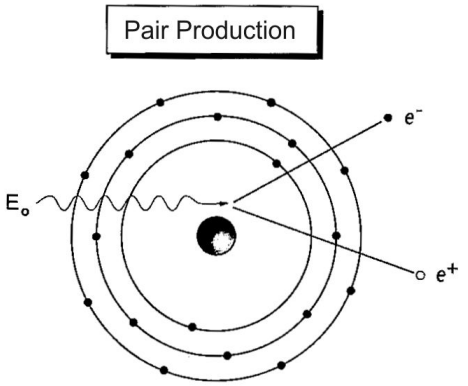

(c) Pair production can occur when an incident x-ray (with E_0 >1.02 MeV) interacts with the electric field of an atom. A negatron (e^-)-positron(e^+) ion pair is formed in the interaction. Pair production does not occus at diagnostic x-ray energies.

Figure A.3 – The three main interactions between x-rays and matter. Reprinted from Beutel et al. [2000].

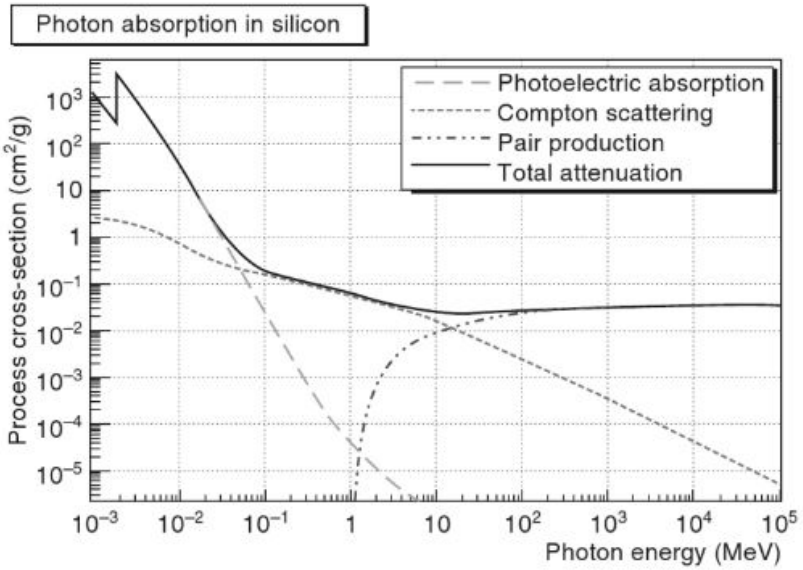

Figure A.4 – Process total cross sections as a function of energy of the impinging radiation in silicon, showing the contributions of the three most common processes: photoelectric absorption, Compton scattering and pair production. [Image from Durini [2014]]

Appendix B

Implemented functionalities

A large part of this research consisted of the implementation of new functions to the existing software to be able to analyse x-ray images. Since the software is meant to be used when the detector is in use, the software should be user-friendly and as complete and ready-to-use as possible, whilst maintaining maximal functionality and versatility. The functionalities implemented for this research will be discussed here, as well as their limitations.

B.1 Region of interest

When a region is selected, the user can choose to get information about that region in two ways. Firstly, the simplest of statistics can be asked from the program. This results in a dialog like the one shown in figure B.1b to appear, on which the mean and standard deviation of the region are given for all available layers. This can be useful when looking at an open beam image (see section 3.1.1).
The user can also choose to get a more detailed look at the distribution of charge (or correspondingly, photons) within the region of interest by looking at the profile of the region in the horizontal (x) or vertical (y) direction. A profile in the x direction means that for each x-value, all values in the column corresponding to that x-value will be added and the resulting value will be plotted in the profile plot. Such profiles can be seen in figures B.1c and B.1d. The profile in the y-direction does not give much information, as expected when looking at the selected region. The dialog in which these profiles appear will be discussed in the next section.

B.2 Profile dialog in depth

The window that appears when the user chooses to plot the profile of the selected region in the x- or y-direction is called the profile dialog as shown in figure B.2. The profile is plotted at the top, with the chosen direction on the horizontal axis and the summed pixel values on the vertical axis. The user can choose to change the vertical axis to a logarithmic scale. The threshold drop down menu allows the user to look at the profiles of data of different thresholds.
To calculate the CNR (see section 3.2) the user can indicate boundary points either by clicking on the profile or typing the values by hand. The user can choose to indicate one or two background regions along with the signal region, the CNR calculation will take this into account. When pressing on the *calculate CNR* button, not only the CNR will be calculated and shown to the user, the program will also show basic statistics on each of the indicated regions. The mean will also be visualised in the plot as red lines across each region. A logarithmic signal-to-noise ratio in units of decibel is also calculated and shown to the user. This however was not of any use for this project, since the CNR gives a much more insightful quantification of the signal.
If the user wants to be consisted throughout measurements, (s)he can choose to use a

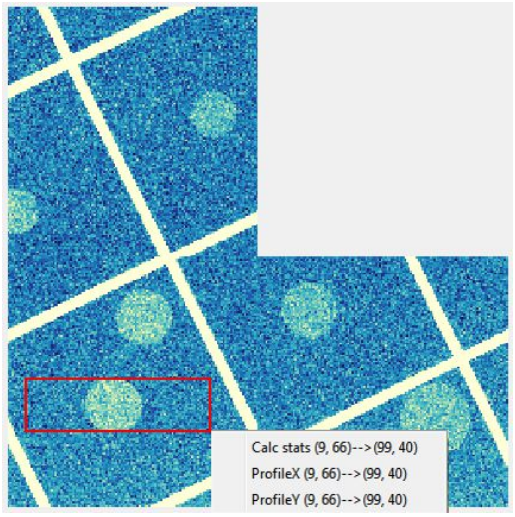

(a) An example of on image with a red square indicating the selected region of interest. The options for the user are shown.

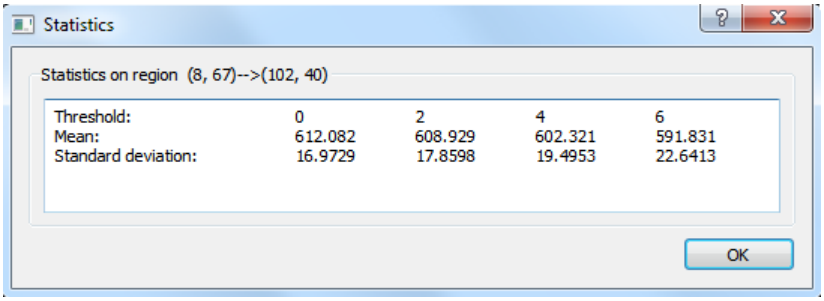

(b) The statistics dialog corresponding to the selected region.

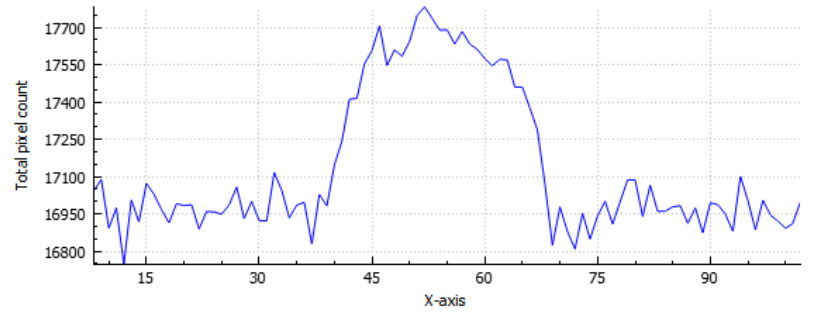

(c) The profile in the x-direction of the selected region.

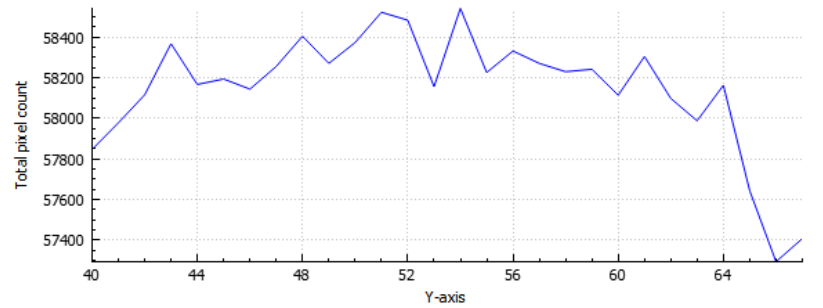

(d) The profile in the y-direction of the selected region.

Figure B.1 – Illustration of the users options when selecting a region.

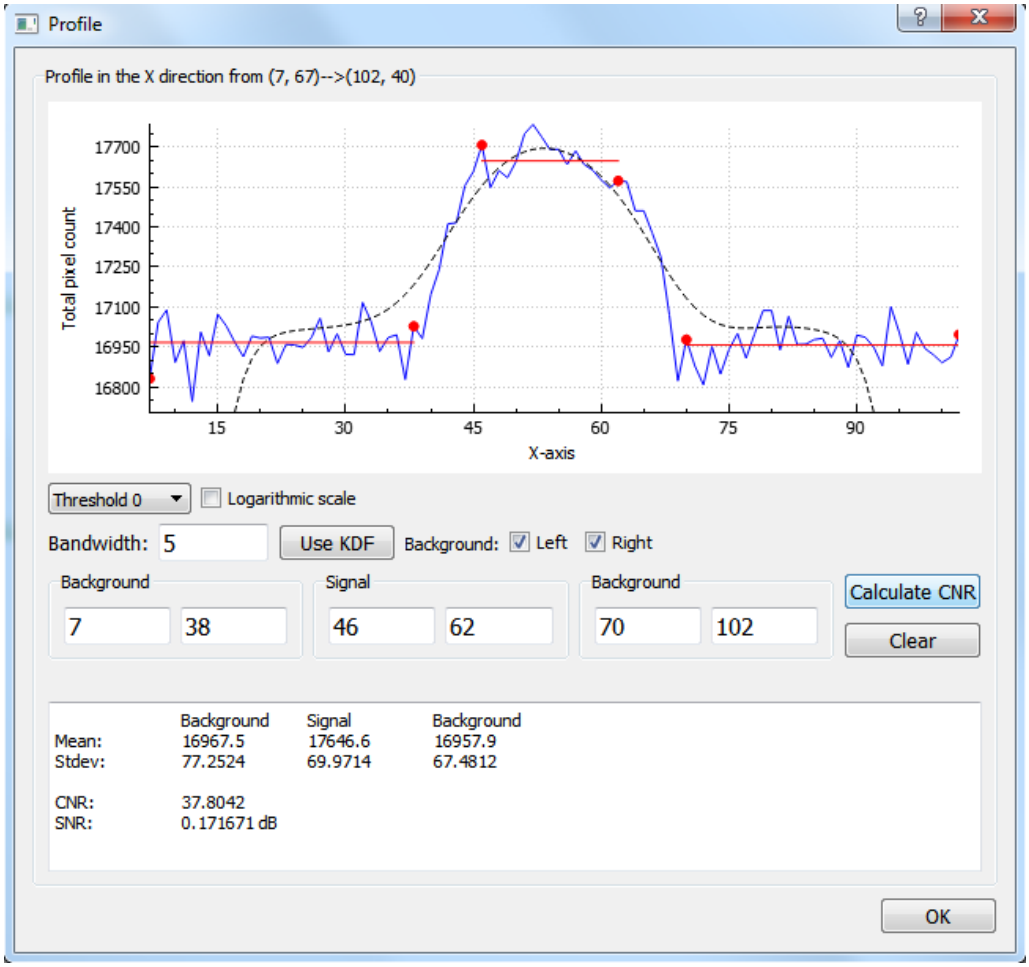

Figure B.2 – The profiledialog in which the KDF function was used and CNR has been calculated.

kernel density function (see section 3.3) to determine the boundary points. This creates a smoothed version of the profile which is shown as a dashed black line in the profile, as can be seen in figure B.2. It is scaled up to lie on approximately the same level as the profile, this is purely for visualisation of the procedure. The actual values of the KDF function do not matter in the determination of the boundary points. The user has to set a bandwidth[1], which is the width of the gaussians that are created for each point. A lower bandwith means the KDF follows the actual shape of the profile more closely. A larger bandwith is more appropriate, since we want to smooth out all bumps untill we only have one left: the main signal.

B.3 Possible improvements and extensions

The KDF procedure only works correctly if a bandwidth is chosen such that there only remain two inflection points. Choosing a smaller bandwidth means the KDF follows the original curve more closely and can result in more than two inflection points. It can be argued that even these smaller bandwidths should be made to work, since the two inflection points of interest often remain at the same positions. This is something that could be implemented. Currently, the code does nothing if there are more than two inflection points.
Furthermore, the KDF procedure can only work with sufficiently large background re-

[1] If it is forgotten, a default value is used.

gions. This is because values of the KDF near the edges have to be discarded (see section 3.3). This sometimes leaves too little of the function left to work with.
Also due to time constraints the two region KDF calculation has not been properly implemented yet. When the regions are sufficiently large the KDF may give reasonable boundary points. Nevertheless, in the cases mentioned above the user is given a warning to adjust the boundary points by hand or choose a larger bandwidth (in the first case).
To make the software more user-friendly, a square indicating the chosen region should be made visible when selecting a region of interest and when an analysis option has already been chosen for that region. Also, when accidentally choosing the wrong analysis axis, the user should be able to switch to the correct one without having to select the exact same region again. This could be implemented very quickly and without any difficulties.